https://doi.org/10.1016/j.optcom.2020.125815

Parity-Time Symmetry Based on Resonant Optical Tunneling Effect for Biosensing

Aoqun Jian,[1,2] Feng Liu,[1,2] Gang Bai,[1,2] Bo Zhang,[1,2] Yixia Zhang,[1,2] Qianwu Zhang,[3] Xiaoming Xue,[4] Shengbo Sang,[1,2,*] and Xuming Zhang,[5,*]

[1]MicroNano System Research Center, Taiyuan University of Technology, Taiyuan 030024, China

[2]Key Laboratory of Advanced Transducers and Intelligent Control System, Shanxi Province and Ministry of Education, Taiyuan 030024, China

[3]Key Laboratory of Specialty Fiber Optics and Optical Access Networks, Shanghai University, Shanghai 200072, China

[4]Department of Respiration, Shanxi Hospital of Traditional Chinese Medicine, Taiyuan 030012, China

[5]Department of Applied Physics, Hong Kong Polytechnic University, Hung Hom, Kowloon, Hong Kong China

Corresponding author: sunboa-sang@tyut.edu.cn (S. Sang), xuming.zhang@polyu.edu.hk (X. M. Zhang)

Abstract: This paper proposes and analyzes a parity-time (PT) symmetry structure based on resonant optical tunneling effect (ROTE) by using two directly coupled ROTE resonators to achieve a balanced gain-loss distribution. The unbroken/broken states of the PT symmetric system are theoretically verified by coupled-mode theory (CMT), transmission matrix method (TMM) and finite-difference time-domain (FDTD). To demonstrate the application potential, we further propose a label-free biosensing scheme that takes advantages of the square-root dependence in frequency splitting near exceptional point (EP). The theoretical results show that the sensor has a maximum sensitivity of 1×10^{5} nm/IP unit (imaginary part unit of refractive index) and a theoretical detection limit of 5×10^{-10} IP unit (corresponds to 0.4 ng carcinoembryonic antigen (CEA)). Compared with the PT systems based on coupled waveguides or resonators, our design has some distinctive features. It is a multi-layer structure and does not need complicated nanoscale fabrication; the liquid samples "flow-through" the sensing region in the mid of PT structure and would greatly enhance the analyte binding efficiency as compared with the common "flow-over" manner. This simple yet highly sensitive platform would find applications in biomedical sensors, drinking water safety, and drug screening.

Keywords: parity-time (PT) symmetry, resonant optical tunneling effect (ROTE), exceptional point (EP), biosensing, carcinoembryonic antigen (CEA)

1. Introduction

In 1998, C. M. Bender creatively proposed the concept of parity-time (PT) symmetry in the field of quantum mechanics [1]. It was proved that the non-Hermitian Hamiltonian of PT-symmetry system can also make the eigenvalues of Schrödinger equation measurable under specified conditions. Due to the challenge of realizing PT-symmetry in experiments, researchers further extended the application fields of PT-symmetry and constructed the PT-symmetry systems using other physical models [2-7].

Optical PT-symmetry, as one of the ten discoveries of physics of the last ten years selected by *Nature Physics* in 2015 [8], has been widely studied in recent years [9-14]. In 2007, R. El-Ganainy *et al.* applied the concept of PT-symmetry to optical field for the first time, and introduced some

properties and conclusions of PT-symmetry of quantum mechanics into coupled waveguides system [15]. In 2009, A. Guo *et al.* experimentally demonstrated the PT-symmetry system and the loss-induced transparency based on the PT symmetric phase transition [16]; and then C. E. Rüter *et al.* realized and observed the PT-symmetry and spontaneous breaking of coupled waveguides system [17]. Although the structure of coupled waveguides is simple, the coupling region of the structure is so dedicated that it requires high-precision fabrication. In 2013, the unidirectional reflectionless phenomenon was experimentally confirmed by the PT symmetric phase transition of the periodically modulated on-chip optical waveguides system [18]. In 2016, Z. J. Wong *et al.* presented the PT symmetry based on the gain-loss modulation using the periodic loss structure of the semiconductor gain waveguide, and observed the coherent laser emission and the coherent absorption at a fixed wavelength [19]. The PT-symmetry systems constructed by the periodic structure are stable, but suffer from the limited choice of fabrication materials because the device needs to satisfy the requirements of both specific refractive index (RI) and gain-loss distributions. In 2014, B. Peng *et al.* [20] and L. Chang *et al.* [21] successively realized optical PT-symmetry in coupled whispering-gallery-mode (WGM) microtoroids and designed an optical isolation by utilizing the nonlinear effect induced by gain amplification. A simple method to obtain the PT-symmetry is to balance the gain and the loss in the coupled resonators system. Due to the extremely high quality factor of WGM microcavity, its loss can be easily compensated by the gain medium. However, high Q resonator is still a challenge of nanofabrication, though significant progresses have been made in integration and package recently.

A series of studies [22-25] pioneered by L. Yang indicate that, at phase transition point of PT-symmetry (i.e., exceptional point, EP), there is a much larger response to external perturbation [26-28]. This unique phenomenon inspires the development of ultrasensitive sensors that break the resolution limitation. For example, using PT-symmetric coupled resonators, the angular velocity [29] and movement [30] can be measured with enhanced sensitivity. W. J. Chen *et al.* demonstrated a multiple-nanoparticle detection scheme based on the PT-symmetric WGM microcavities [31], which exhibited a square-root dependence of the frequency splitting to perturbation strength of nanoparticles at the EP. Particularly, the third-order EP, at which the even higher sensitivity is proportional to the cube root of the perturbation strength, was exploited for thermal sensing [32].

On the other hand, resonant optical tunneling effect (ROTE), referring to the resonances of evanescent light in a special five-layer dielectric structure, has its own characteristics. In 1988, Yeh discovered this special phenomenon [33]. In 1999, Hayashi designed a multi-layer structure between Al (or Al_2O_3) and SiO_2 layers on the SF10 glass substrate, and observed the resonance phenomenon by changing the incident angle [34]. In 2005, Yamamoto applied ROTE to an all-optical switch [35]. Our group conducted theoretical studies about ROTE and explored its applications such as RI sensors [36], thermo-optic switches [37] and MEMS accelerometers [38]. Recently, an ROTE-based volume RI sensor was proposed to solve the long-standing problem that the classical sensors based on evanescent field has limited spatial range of measurement so that they cannot measure the entire biological sample with certain size (e.g., eukaryotic cells at 10–100 μm) or the samples/particles naturally suspended in the solution [39]. Experimental studies demonstrated a highly-sensitive detection of hepatoma cell concentrations with the achieved performance among the best.

In this paper, we will construct a PT-symmetry system using two directly-coupled ROTE units and will explore its application as a biosensor with ultrahigh sensitivity. Analysis and simulation will be conducted to verify the PT-symmetry under certain conditions. The square-root response of the

PT-symmetry structure near the EP will be utilized for the detection of biological analytes, and the performance such as sensitivity and detection limit will be estimated. Compared with other PT systems based on coupled resonators, the ROTE-based PT-symmetric system is an essential multi-layer structure and can be fabricated with simple process with low cost. Since the liquid sample flows through the mid of the system, the sample load manner is transferred from the "flow-over" mode to the "flow-through" mode, which enables shorter response time for the sample with low concentration [40-42].

2. Concept and device design

Originated from the optical tunneling effect (i.e., frustrated total internal reflection, FTIR), the ROTE briefly refers to the resonance effect of the tunneled light in a well-designed resonator as shown in Fig. 1(a). Its structure consists of five layers with an alternate high-low distribution of RI, which are named along the light propagating direction as follows: the input layer, the first tunneling gap, the central slab, the second tunneling gap, and the output layer. It is seen that the ROTE resonator is a multi-layer structure, except for the two non-layered prisms that are for light leading in/out. The ROTE-based PT-symmetry system is designed by directly coupling 2 units of ROTE resonators as illustrated in Fig. 1(b). The first ROTE resonator (i.e., gain cavity) is doped Er^{3+} ions to provide the optical gain using a pump laser (980 nm). The other resonator (i.e., loss cavity) is made of low-absorption silicate glass. They all belong to low dispersion glass (The abbe number is 77), where the causality and Kramers-Kronig can be satisfied [14,43] and the PT-like threshold behavior can be observed [44]. The coupling strength of these two cavities can be tuned by adjusting the gap (i.e., coupling layer) between them. For our device, the materials and parameters are listed in TABLE I. The choice of parameters ensures a resonant mode in both the gain and loss cavities in the 1535 nm band of the probe light. However, the mode of 980 nm band light can not be supported by the loss cavity. Therefore, the pump light only resonates in the gain cavity.

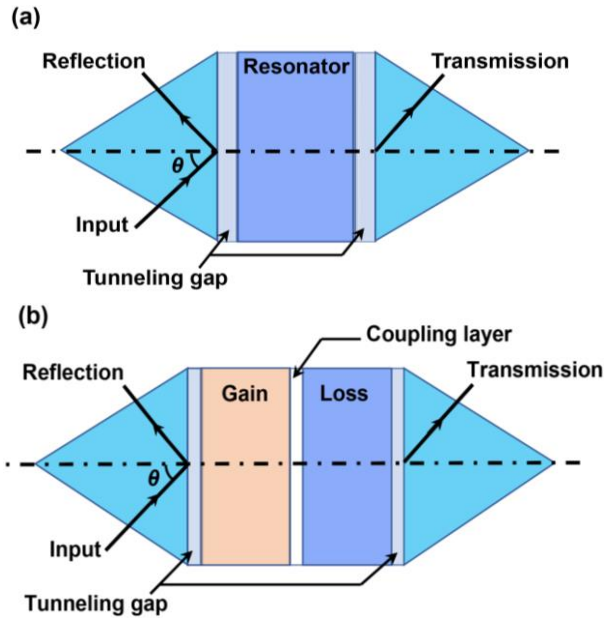

Fig. 1. Schematic designs of the ROTE resonator (a) and the ROTE-based PT-symmetry system (b).

TABLE I Materials and design parameters of the ROTE-based PT-symmetry system

Parameter	Material	Symbol	Value
RI of input prism	K9 glass	n_{in}	1.5000-9.84×10^{-8} i
RI of the first tunneling layer	Polydimethylsiloxane(PDMS)	n_1	1.3960-5.2×10^{-6} i
Width of the first tunneling layer		d_1	6μm
RI of gain cavity	Er^{3+} doped phosphosilicate	n_{gain}	1.5240+1.2627×10^{-7} i
Width of gain cavity		d_{gain}	940μm
RI of coupling layer	Sample	n_{samp}	1.3506-6.4538×10^{-5} i
Width of coupling layer		d_{samp}	4.4μm
RI of loss cavity	Low-absorption silicate glass	n_{loss}	1.5238-8.924×10^{-8} i
Width of loss cavity		d_{loss}	942.0715μm
RI of the second tunneling layer	Polydimethylsiloxane(PDMS)	n_2	1.3960-5.2×10^{-6} i
Width of the second tunneling layer		d_2	6μm
RI of output prism	K9 glass	n_{out}	1.5000-9.84×10^{-8} i
Incident angle		θ	69°

As a multi-layer structure, this system can be fabricated easily by simple layer deposition process (e.g., spin coating, sputtering), without the need for the complicated and costly nanofabrication. In our ROTE-based PT-symmetry system, the gain (or loss) cavity can be obtained by Er^{3+} doping (or standard glass). Then, the tunneling layers (i.e., the PDMS layers) with designed thickness can be formed on the surface of gain (or loss) cavity by spin coating. Next, the two cavities can be connected to the input/output prisms by using UV-curing optical adhesive, forming the left/right components. Finally, these two units can be placed on the micro-positioners, respectively. Their coupling strength can be tuned by adjusting the gap between them (i.e., the coupling layer).

3. Theoretical analysis

In order to directly elaborate the physical mechanism of the designed structure, the PT-symmetry structure is considered as a coupled-resonators model (as shown in Fig. 2.). Based on the coupled-mode theory (CMT) [21, 45], the dynamic equation of the probe light for two directed coupled gain and loss cavities of system can be written as follows:

$$\begin{cases} \dfrac{da_1}{dt} = (i\Delta\omega_1 + g)a_1 + i\kappa_0 a_2 + \kappa s_+ \\ \dfrac{da_2}{dt} = (i\Delta\omega_2 - \gamma)a_2 + i\kappa_0 a_1 \end{cases} \tag{1}$$

where a_1 and a_2 are the normalized field amplitudes of probe light in the gain and loss cavities, respectively; $\Delta\omega_{1,2} = \omega - \omega_{1,2}$ are the detunings between the resonant frequencies $\omega_{1,2}$ of the cavities and the frequency ω of probe light; $g = g' - \dfrac{1}{\tau_1} - \dfrac{1}{\tau_{e1}}$ and $\gamma = \dfrac{1}{\tau_2} + \dfrac{1}{\tau_{e2}}$ are the net gain of gain cavity and the loss of loss cavity, respectively, where g' is the gain provided by doped Er^{3+} ions, $\dfrac{1}{\tau_1}$ and $\dfrac{1}{\tau_2}$ are the intrinsic losses of the gain and loss cavities, respectively; $\dfrac{1}{\tau_{e1}}$ and

$\frac{1}{\tau_{e2}}$ are the additional rates of decay due to escaping power for the gain and loss cavities; κ_0 is the coupling strength of the cavities; $\kappa = \sqrt{\frac{2}{\tau_{e1}}}$ is a coefficient expressing the degree of coupling between the resonator and the wave s_+; $|s_+|^2$ is the input power of probe light (Fig. 2.).

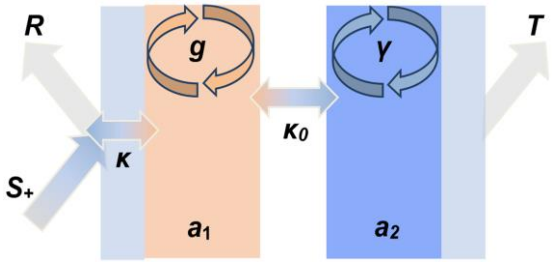

Fig. 2. Schematic graph of the theoretical analys is model based on the CMT. s_+: the field amplitude of probe light; *R*: reflectance; κ: the coupling strength between the gain cavity and external excitation source; *g*: the net gain of gain cavity; γ: the loss of loss cavity; κ_0: the coupling strength of gain and loss cavity; $a_{1,2}$: the normalized field amplitudes of probe light in gain and loss cavities; *T*: transmittance.

When the system is in steady state and κs_+ is neglected, the eigenfrequencies $\omega_\pm$ of the two supermodes of this system are given by:

$$\omega_\pm = \frac{\omega_1 + \omega_2}{2} + i\frac{g-\gamma}{2} \pm \sqrt{{\kappa_0}^2 + (\frac{\omega_1 - \omega_2}{2} + i\frac{g+\gamma}{2})^2} \tag{2}$$

If the system satisfies the PT-symmetry condition and the resonant frequencies of cavities are equal, which means $g = \gamma$ and $\omega_1 = \omega_2$, then the eigenfrequencies are written as:

$$\omega_\pm = \omega_0 \pm \sqrt{{\kappa_0}^2 - \gamma^2} \tag{3}$$

where $\omega_0 = \omega_1 = \omega_2$ and ω_0 is the central frequency.

Further simplification of Eq. (3) yields:

$$\Delta\omega = \pm\sqrt{{\kappa_0}^2 - \gamma^2} \tag{4}$$

Therefore, if the coupling strength is greater than the total loss of the system, which means $\kappa_0 > \gamma$, then the eigenfrequencies $\omega_\pm$ are real numbers that sit at distances of $\sqrt{{\kappa_0}^2 - \gamma^2}$ away from the central frequency ω_0, resulting in two peaks in the output spectrum. Here we define the

difference between eigenfrequencies as the "spectral distance". In case of $\kappa_0 = \gamma$, the eigenfrequencies coalesce at the central frequency ω_0, causing the two peaks to merge into one. On the other hand, if the coupling strength is less than loss (i.e., $\kappa_0 < \gamma$), then the eigenfrequencies become imaginary numbers and result in only one peak in the output spectrum, which shows that the PT-symmetry is broken. Thus, the condition of $\kappa_0 = \gamma$ is just the EP that marks the critical state of PT-symmetry breaking [46].

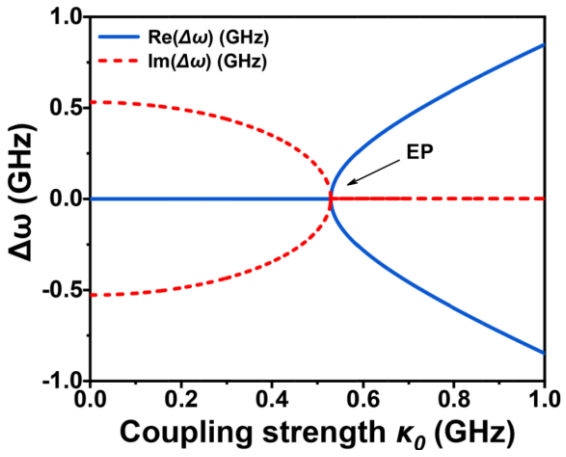

Fig. 3. Evolution of Real (blue solid line) and imaginary (red dashed line) parts of $\Delta\omega$ with respect to coupling strength in the ideal PT-symmetry system. The values of the involved parameters are listed as follows: $\omega_1 = \omega_2$ =195390×2π GHz; $1/\tau_1$ =0.0155×2π GHz; $1/\tau_{e1}$ =0.1439×2π GHz; $\gamma = 1/\tau_2 + 1/\tau_{e2}$ =0.0840×2π GHz; g' =0.2390×2π GHz.

The numerical results of the real part $\mathrm{Re}(\Delta\omega)$ and the imaginary $\mathrm{Im}(\Delta\omega)$ as a function of coupling strength κ_0 are plotted in Fig. 3. When κ_0 is greater than the EP, which means the system is in the unbroken PT-symmetry state (i.e., the strong coupling region), the difference of the real part increases gradually with the coupling strength but the imaginary part is always 0. Oppositely, when κ_0 is less than the EP (i.e., the broken PT-symmetry state, the weak coupling region), the difference of the real part is always 0 but the imaginary part increases gradually with weaker coupling strength.

Next, the influences of gain on the output spectrum are investigated. When the system is in the steady state, the formula (1) can be written as:

$$\begin{cases} (i\Delta\omega_1 + g)a_1 + i\kappa_0 a_2 + \kappa s_+ = 0 \\ (i\Delta\omega_2 - \gamma)a_2 + i\kappa_0 a_1 = 0 \end{cases} \tag{5}$$

So a_1 can be expressed as:

$$a_1 = \frac{\kappa(\gamma - i\Delta\omega_2)s_+}{\kappa_0{}^2 + (i\Delta\omega_1 + g)(i\Delta\omega_2 - \gamma)} \tag{6}$$

Therefore, the reflectance (i.e., the amplitude of output spectrum) can be written as [20-21, 24]:

$$R = \left|1 - \kappa\frac{a_1}{s_+}\right|^2 = \left|1 - \frac{\kappa^2[\gamma - i(\omega - \omega_2)]}{\Gamma(\omega)}\right|^2 \tag{7}$$

where $\Gamma(\omega) = (i\Delta\omega_1 + g)(i\Delta\omega_2 - \gamma) + \kappa_0{}^2$.

It can be seen from Eq. (7) that the resonant frequency has a notable influence on output spectrum. The amplitudes of super modes are related to the difference between ω_1 and ω_2. When the amplitudes are equal, the resonant frequencies would be identical. As shown in Fig. 4(a), under the strong coupling condition, as g' increases from zero, the downward double-peak has a decreasing depth and then turns into the upward double-peak. With continuous increase of g', the amplitude of double-peak increases gradually; at $g' = \frac{1}{\tau_1} + \frac{1}{\tau_2} + \frac{1}{\tau_{e1}} + \frac{1}{\tau_{e2}}$, which means $g = \gamma$, the amplitude reaches the maximum and then begins to decrease if g' continues to increase. The condition called strong coupling is far from EP, indicating that the change of spectral distance is insensitive and the effect of gain on spectrum is mainly shown within spectral amplitude instead of spectral distance. Therefore, the change of the amplitude of double-peak can be utilized to determine whether the system reaches the balanced gain and loss, which is considered to be a criterion of the PT-symmetry in our system [21, 47].

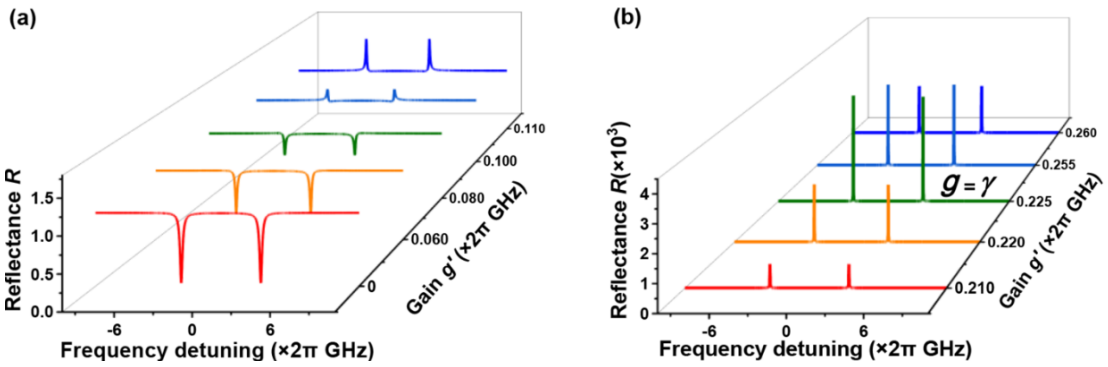

Fig. 4. Variation of the output spectrum with the increase of net gain as calculated using the coupled-mode theory. (a) When the net gain increases from zero, the downward double-peak becomes shallow and then turns into the upward double-peak. (b) When the net gain increases continuously, the double-peak increases gradually in amplitude until it reaches the maximum and then begins to decrease. In this analysis, κ_0 =3.1713×2π GHz, and the values of other parameters are specified in accordance with those participated in Fig. 3.

To verify the results given by the CMT, the transmission matrix method (TMM) is adopted to calculate the output spectrum of the ROTE-based PT-symmetry system [33]. The values of the related parameters are listed in Table Ⅰ. As shown in Fig. 5, when the gain (i.e., the positive imaginary part of RI) of the gain cavity goes stronger, the double-peak of output spectrum exhibits a similar trend as predicted by the CMT. The inequality between two peaks is caused by the significant effect of the coupling layer's absorption. When the system is in the PT-symmetry state, the output spectrum varies with the change of the width of coupling layer as plotted in Fig. 6. Wider coupling layer causes the output peaks to gradually approach each other and to ultimately merge into one. In other words, the increase of the coupling layer width causes the system to enter into the broken state.

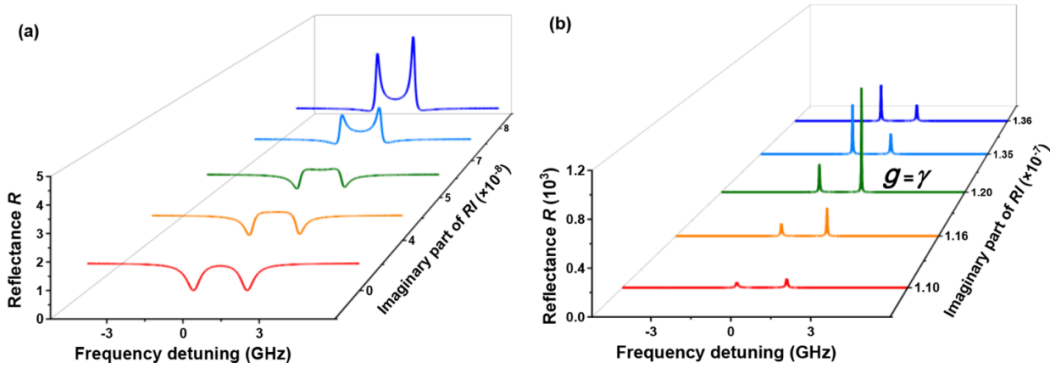

Fig. 5 Output spectrum of the ROTE-based PT-symmetry system as a function of the net gain as predicted by the transmission matrix method (TMM). (a) When the imaginary part of RI increases gradually from zero, the depth of the downward double-peak of output spectrum becomes shallow and then transits to the upward double-peak. (b) When the imaginary part of RI increases continuously, the amplitude of double-peak increases gradually until reaches the maximum and then begins to decrease.

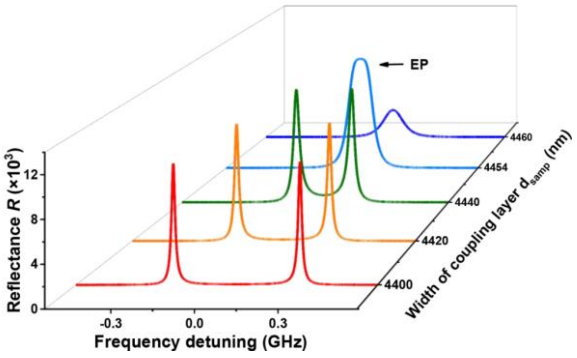

Fig. 6. Illustration of the switch from the PT-symmetry state to the breaking state. When the system is in the unbroken PT-symmetry regime, the spectral distance decreases with the increase of the width of coupling layer (i.e., the decrease of coupling strength). Then, when the width of coupling layer reaches a special value, the double-peak would be changed into the single-peak, representing the start of a broken state of the system. Finally, the amplitude of single-peak would drop with the further increase of the width of coupling layer.

For further verification, the electric field distributions below and above the critical value of PT-symmetry breaking are simulated using the finite-difference time-domain (FDTD) method as presented in Fig. 7. In order to save the simulation resource and time, the system is simplified, the related parameters of the simulated structure are provided (see S1 in "Supplementary Material"). When

the system is in the unbroken state (Fig. 7(a), (b)), the supermodes are evenly distributed in the gain and loss cavities. For the supermode of smaller wavelength, the intensity in coupling layer is low (see Fig. 7(a)); for longer wavelength, the intensity in coupling layer becomes larger (see Fig. 7(b)). In contrast, when the coupling strength exceeds the critical value of PT-symmetry breaking (Fig. 7(c)), the supermode experiences an amplification process in gain cavity while the other fades significantly due to the attenuation. The locations of supermodes are indicated in Fig. 7(d). This phenomenon is consistent well with the reported simulation results and experimental observations of the PT-symmetry structures based on coupled WGM microcavities [43, 48].

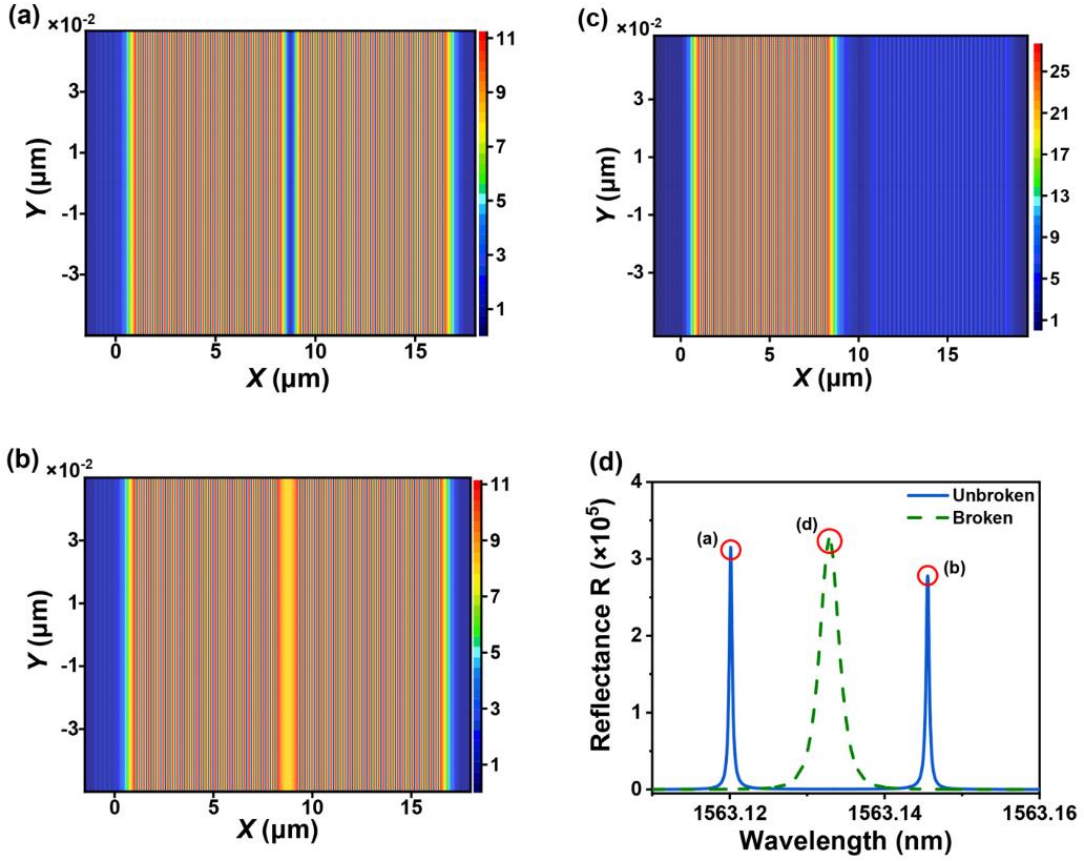

Fig.7. Simulated electric field distribution below ((a) and (b)) and above (c) the critical value of PT-symmetry breaking. (d) Indication of the supermodes in the reflection spectrum.

4. Biosensor based on nanoparticle detection

4.1 Theoretical analysis

When nanoparticles are bound to the surface of gain cavity, the perturbation strength ε is introduced in the system, Eq. 1 is rewritten as:

$$\begin{cases} \dfrac{da_1}{dt} = (i\Delta\omega_1 + g - \varepsilon)a_1 + i\kappa_0 a_2 + \kappa s_+ \\ \dfrac{da_2}{dt} = (i\Delta\omega_2 + \gamma)a_2 + i\kappa_0 a_1 \end{cases} \tag{8}$$

Then, the eigenfrequencies are rewritten as:

$$\omega_{\pm} = \frac{\omega_1 + \omega_2}{2} + i\frac{g - \varepsilon - \gamma}{2} \pm \sqrt{\kappa_0{}^2 + (\frac{\omega_1 - \omega_2}{2} + i\frac{g - \varepsilon + \gamma}{2})^2} \tag{9}$$

When $g = \gamma$ and $\omega_1 = \omega_2$, the detunings between the eigenfrequencies and the central frequency are:

$$\Delta\omega = -i\frac{\varepsilon}{2} \pm \sqrt{\kappa_0{}^2 - (\gamma - \frac{\varepsilon}{2})^2} \tag{10}$$

where $-i\frac{\varepsilon}{2}$ is the mode attenuation of eigenfrequencies. With the perturbation, the position of EP is shifted and causes an apparent splitting of $\mathrm{Re}(\Delta\omega)$ at the original EP as shown in Fig. 8.

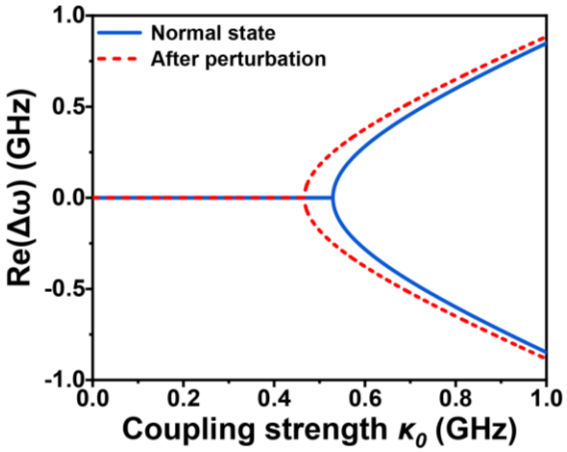

Fig. 8. Evolution of $\mathrm{Re}(\Delta\omega)$ with respect to the coupling strength before (blue solid line) and after (red dashed line) the introduction of perturbation. In this calculation, ε =0.02×2π GHz, and the values of other parameters are same as those participated in Fig. 3.

Now we turn to study the shifts of eigenfrequencies at the EP after the perturbation. Eq. 10 can be simplified as:

$$\Delta\omega = -i\frac{\varepsilon}{2} \pm \sqrt{\gamma\varepsilon - \frac{\varepsilon^2}{4}} \tag{11}$$

If the perturbation is sufficiently small, which means $\varepsilon << \gamma$, then $\Delta\omega = -i\frac{\varepsilon}{2} \pm \sqrt{\gamma\varepsilon}$.

Therefore the difference of $\mathrm{Re}(\Delta\omega)$ (i.e., $2\sqrt{\gamma\varepsilon}$) is proportional to the square-root of perturbation, which implies that smaller perturbation enjoys higher sensitivity. This encouraging result is quite similar to the result proposed by L. Yang *et al* [31].

4.2 Biosensor structure design

To explore the application of ROTE-based PT-symmetry system, a biosensor is proposed for specific label-free detection of biological analytes as shown in Fig. 9. The sensor is based on the PT-symmetry

system, the gap (i.e., the coupling layer) between the gain cavity and the loss cavity can be used as the microchannel to load the gas or liquid samples. The surface of gain cavity is biofunctionalized in advance so as to bind specific target analytes, such as DNA, protein, polysaccharide, etc. To further demonstrate the application potential of the designed sensor, carcinoembryonic antigen (CEA) is used as the analyte of interest and the sensing performance is evaluated. Early diagnosis of lung cancer (ultra-low concentration CEA detection) is crucial to the five-year survival rate of patients, and CEA is one of the most important analytes for the diagnosis of lung cancer in recent years. For CEA, Staphylococcal Protein A (SPA), which is capable of specifically binding to the antibodies on the sensing surface, has a main role in the immobilization of the capture antibody. Then the antigen-antibody specific binding is utilized to capture CEA from the loaded exhaled breath condensate (EBC) sample [49, 50]. In our design, all the target analytes are loaded into a small confined space and flowed through the narrow sensitive region. The sample load manner is shifted from the "flow-over" mode to the "flow-through" mode. For "flow-over" scheme, the sample load relies on the the analytes in bulk solution to diffuse to the sensing surface. In the case of 'flow-through' strategy, micro/nanofluidic channels employed for sample deliver are integrated through the optical sensing structure, so that the entire sample flow is directed towards the sensing surface [40-42]. The sample is delivered mostly by "convection" (or "convective diffusion") rather than the "diffusion", which can significantly improve the binding efficiency of analytes and reduce the response time of the sensor.

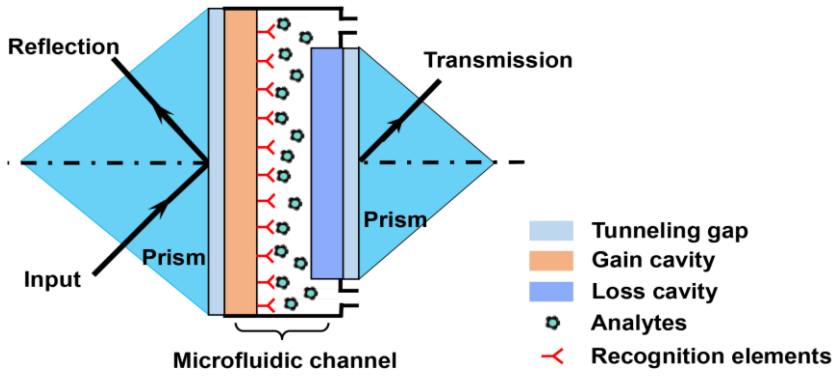

Fig. 9. Schematic diagram of the biosensor structure using the ROTE-based PT-symmetry system. The coupling layer between the gain cavity and the loss cavity acts as a microfluidic channel to load analytes.

4.3 Sensing mechanism and performance evaluation

According to the theoretical analysis, if the system is at EP, the increase of absorption of gain cavity would lead to the splitting of the output spectrum from single-peak to double-peak. Fig. 10 shows the splitting process of output spectrum from a single-peak to a double-peak at the EP as the absorption coefficient of the gain cavity goes up in response to the binding of biological analytes on the surface of gain cavity. The relationships between the spectral distance and the sensitivity with respect to the absorption of gain cavity are plotted in Fig. 11. At the EP, if the imaginary part of RI of gain cavity is increased from the EP by 5×10^{-10}, the single-peak begins to split into the double-peak with a spectral distance of 0.09 pm; the corresponding sensitivity of the sensor (i.e., spectral distance per absorption unit) reaches above 1×10^{5} nm/IP unit (Imaginary Part unit of RI). Stronger absorption of gain cavity leads to a continuous increase of the spectral distance (see the blue line in Fig. 11 (a)); however, the

sensitivity gradually goes down but it still remains 4×10^4 nm/IP unit (see the red line in Fig. 11 (a)). And the square-root dependence of the splitting spectral distance on the absorption of gain cavity is confirmed by the log-log plot with a linear slope of 1/2 in Fig. 11 (b). The spectrum splitting and the trend of sensitivity variation in the system are similar to those of the other PT-symmetry based sensing systems as proposed by W. J. Chen *et al.* [31] and H. Hodaei *et al.* [32].

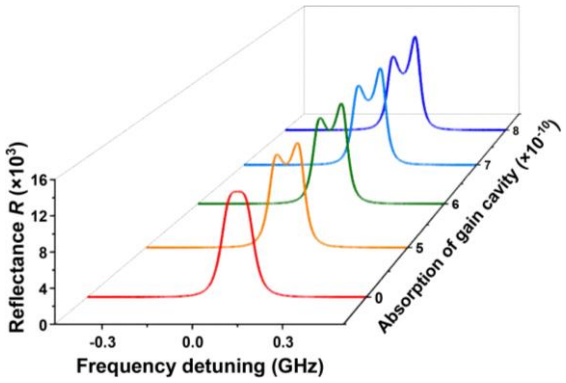

Fig. 10. Splitting process of the output spectrum with the increase of the absorption of gain cavity.

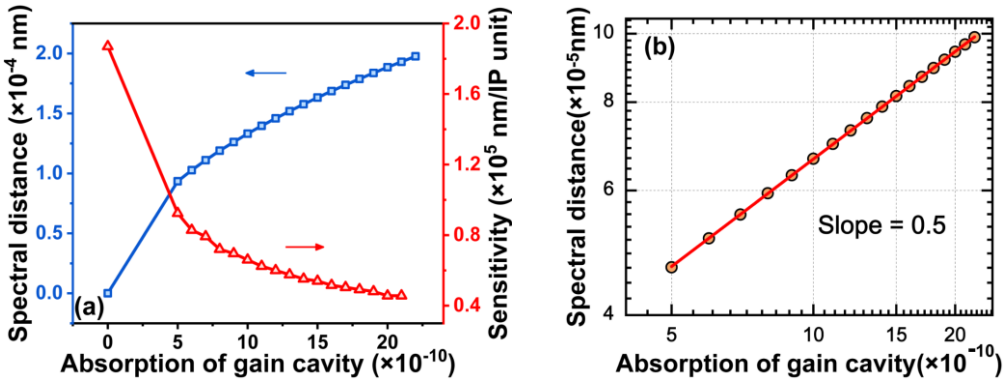

Fig. 11. (a): Spectral distance (left Y axis, blue line) and sensitivity (right Y axis, red line) with respect to the absorption of gain cavity as represented by imaginary part of RI of gain cavity. Stronger absorption causes a gradual increase of the spectral distance (Left) and a decay of the sensitivity from 1×10^5 nm/IP unit to the flat level at 1×10^4 nm/IP unit. (b): The log-log plot of the dependence of the splitting spectral distance on the absorption of gain cavity, where a linear slope of 1/2 can be obtained.

On the other hand, when the sample is loaded and flowed through the coupling layer and the target analytes are bound to the surface of the gain cavity, the RI and absorption of coupling layer will also change due to the volume concentration variation of the analyte. As is shown in Fig. 12(a), the output spectrum will also split from a single-peak to a double-peak at EP with the change of RI of biological analytes locating in coupling layer, from which we can see that the output spectrum simultaneously has a red shift in the process of splitting. And the Fig. 12(b) shows the effect of the RI of biological analytes on the output spectrum at EP. When the RI of biological analytes increases gradually, the single-peak begins to split and the spectral distance increases gradually. However, the simulation results show that the distance is insensitive to RI of the analytes, and the sensitivity is less than 6 nm/RIU (Refractive Index Unit), which is about 10^{-5} of the sensitivity due to the absorption. Furthermore, as the concentration of the loaded analyte is tiny (e.g. the typical CEA density in a human

EBC sample is ng/ml level [51]), the range of the volume concentration variation is limited, of which impact on the the output spectrum near EP is negligible. The influence of the absorption decrease of coupling layer on the reflection spectrum is presented in Fig. 13. It can been seen that, as the imaginary part of RI of coupling layer drops from the EP by 4×10^{-6} (10^4 times larger than the change of gain cavity in Fig. 11), only the left shoulder of the peak grows significantly and no obvious splitting can be observed. Therefore, compared with the change of absorption induced by the biological binding, such RI and absorption variation of the coupling layer has limited impact on the PT-symmetry state based on our investigation.

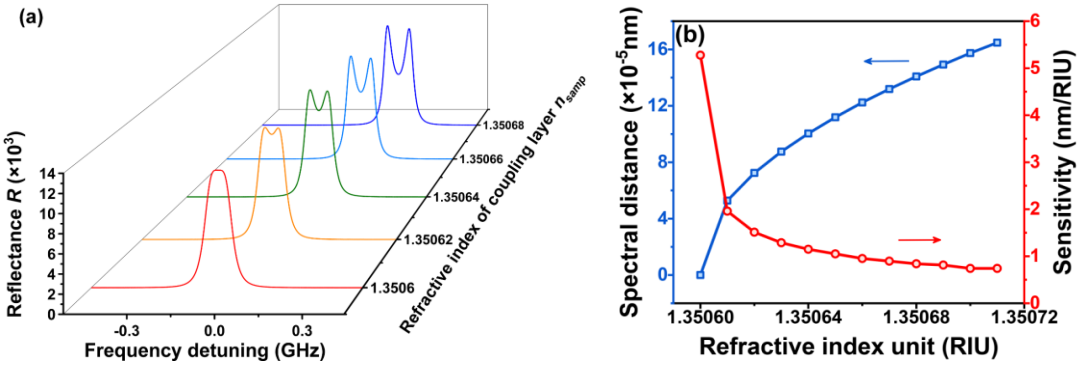

Fig. 12. (a): The splitting process of output spectrum with the RI changing of coupling layer. (b): The change of spectral distance and sensitivity with respect to the RI of coupling layer. On the one hand, with the increasing of RI of analytes, the spectral distance increases gradually in nonlinearity; on the other hand, with the increases of RI of analytes, the sensitivity decreases and the maximum is less than 6 nm/RIU.

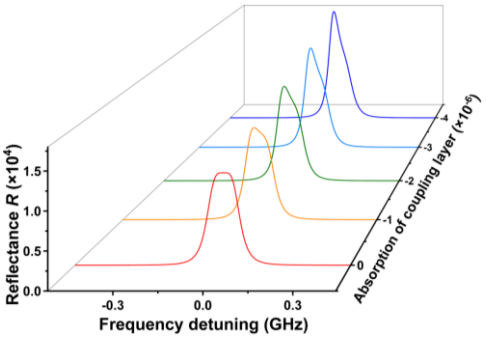

Fig. 13. The variation of reflection spectrum with the absorption decrease of coupling layer.

According to the simulation results and the Rayleigh criterion (the minimum resolvable spectral distance is equal to the full width at half maximum), the resolution of the sensor system to the imaginary part of RI can reach 5×10^{-10} IP unit, corresponding to an absorption coefficient 4×10^{-5} cm^{-1}. If the length of the cavity is 940μm, the total absorption of the gain cavity that can be distinguished is 3.76×10^{-6}. On the other hand, assuming the cross-section of gain cavity is 0.25 cm^2, if 1 g CEA is all deposited on the gain cavity, its thickness would be 3 cm (the density is about 1.35×10^3 kg/m^3). As the molar extinction coefficient of CEA is 1×10^5 M^{-1} cm^{-1} [52], the absorption of CEA per unit length (1 cm) is 3.3×10^4 cm^{-1}(not including optical scattering or dispersion). Based on the simulation results, the minimum thickness of CEA can be detected is 1.13×10^{-10} cm, which corresponds to 0.4 ng

(equivalent to 2.2 fmol). The typical amount of CEA for detection is 4~8 ng (the CEA concentration in exhaled breath condensate (EBC) is about 2 ng/ml for health patients and > 4 ng/ml for lung cancer patients, and a typical sample volume of EBC is 2 ml), which is much larger than the theoretical detection limit (i.e., 0.4 ng) of the sensor. Since the sample flow with target analyte can be circulated in a well-designed microfluidics system of the device, the amount of CEA captured by the recognition elements can be cumulative on the surface of gain cavity. By reasonably controlling the flow rate of the EBC sample, the designed sensor has the potential to detect CEA at ultra-low concentration with high sensitivity. Due to the square-root dependence of the system sensitivity to the perturbation strength, the designed sensor has a low linearity, but it can be solved by signal processing procedure (e.g. intelligent searching from the recorded datasets obtained from previous calibration). And although quantum noise should be taken into consideration to assess the ultimate performance of the EP sensors [53], the parametrically improved signal-to-noise ratio can be achieved by using a specific experimental protocol [54].

Some parametric studies have been carried out to characterize the performance of the sensor with respect to the critical dimensions of the sensor structure. The results are plotted in Fig. 14. When the width of tunneling layer increases, the system needs a smaller critical gain value (i.e., a critical value of imaginary part of RI of gain cavity) to realize the PT-symmetry, and the width of the coupling layer goes larger at the EP, which are beneficial to the experiment. However, the spectral distance would drop, causing a lower sensitivity of the designed sensor. In real experiment, the system detection limit will be subject to a variety of factors such as the *Q* factor of resonators, the noise level of the whole system, and so on.

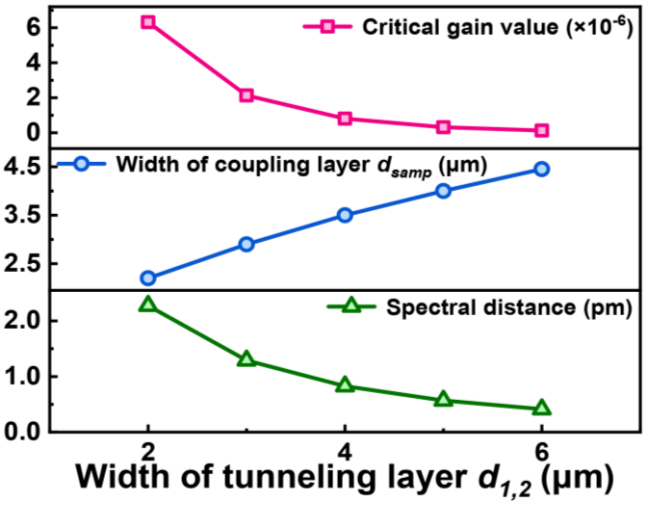

Fig. 14. Influence of the width of tunneling layer on the critical gain value, the width of coupling layer and the spectral distance. When the width of tunneling layer increases gradually, the critical gain value for the PT-symmetry goes down, the width of coupling layer for the EP increases but the spectral distance gets smaller.

5. Conclusions

In summary, the ROTE-based PT-symmetry system has been proposed and evaluated for biosensing. The output spectrum of the system with respect to the gain and the couple strength is analyzed by using the coupled-mode theory and the transfer matrix method. The results are mutually verified and the PT-symmetry is theoretically confirmed when the gain and the loss are balanced. The electric field distribution below/above the critical state of PT-symmetry breaking is provided as an evidence of

PT-symmetry breaking. Based on the PT-symmetry system, a label-fee biosensor is constructed and its performance is theoretically estimated. The splitting of peak occurs at the EP after the introduction of the perturbation, and a smaller perturbation produces a larger sensitivity. The analysis shows that the sensor has a theoretical detection limit of 5×10^{-10} IP unit (corresponding to 0.4 ng or 2.2 fmol of CEA) and the maximum sensitivity is 1×10^{5} nm/IP unit. Our work provides a feasible method for the detection of particles with low concentration and would find useful applications in biomedical diagnosis, drinking water safety, drug screening and environment protection.

Funding. This study was financially supported by the National Natural Science Foundation of China (No. 61971301, 61471255, 61474079, 51622507 and 61377068), 863 project (2015AA042601), Excellent Talents Technology Innovation Program of Shanxi Province (201805D211021), and Research Grants Council of Hong Kong (N_PolyU505/13, 152184/15E, 152127/17E and 152126/18E).

Disclosures. The authors declare that there are no conflicts of interest related to this article.

REFERENCES

[1]. C. M. Bender, S. Boettcher, Real Spectra in Non-Hermitian Hamiltonians Having PT Symmetry, Phys. Rev. Lett. 80, (1998) 5243-5246.

[2]. R. Fleury, D. Sounas, A. Alu, An invisible acoustic sensor based on parity-time symmetry, Nat. Commun. 6, (2015) 5905.

[3]. J. Schindler, A. Li, M. C. Zheng, F. M. Ellis, T. Kottos, Experimental Study of Active LRC Circuits with PT-Symmetries, Phys. Rev. A. 84, (2011) 040101.

[4]. N. Bender, S. Factor, J. D. Bodyfelt, H. Ramezani, D. N. Christodoulides, F. M. Ellis, T. Kottos, Observation of asymmetric transport in structures with active nonlinearities, Phys. Rev. Lett. 110, (2013) 234101.

[5]. M. Znojil, PT-symmetric square well, Phys. Lett. A. 285, (2001) 7-10.

[6]. P.-Y. Chen, M. Sakhdari, M. Hajizadegan, Q. Cui, M. M.-C. Cheng, R. El-Ganainy, A. Alù, Generalized Parity-Time Symmetry Condition for Enhanced Sensor Telemetry, Nat. Electron. 1, (2018) 297-304.

[7]. Z. Y. Gu, N. Zhang, Q. Lyu, M. Li, S. M. Xiao, Q. H. Song, Experimental demonstration of PT-symmetric stripe lasers, Laser Photonics Rev. 10, (2016) 588-594.

[8]. J. Cham, Top 10 physics discoveries of the last 10 years, Nat. Phys. 11, (2015) 799-799.

[9]. M. A. Miri, A. Alu, Exceptional points in optics and photonics, Science 363, (2019) eaar7709.

[10]. L. Feng, R. El-Ganainy, L. Ge, Non-Hermitian photonics based on parity–time symmetry, Nat. Photon. 11, (2017) 752-762.

[11]. R. El-Ganainy, K. G. Makris, M. Khajavikhan, Z. H. Musslimani, S. Rotter, D. N. Christodoulides, Non-Hermitian physics and PT symmetry, Nat. Phys. 14, (2018) 11-19.

[12]. S. V. Suchkov, A. A. Sukhorukov, J. Huang, S. V. Dmitriev, C. Lee, Y. S. J. L. Kivshar, P. Reviews, Nonlinear switching and solitons in PT-symmetric photonic systems, Laser Photon. Rev. 10, (2016) 177-213.

[13]. H. Zhao, L. Feng, Parity–time symmetric photonics, Natl. Sci. Rev. 5, (2018) 183-199.

[14]. A. A. Zyablovsky, A. P. Vinogradov, A. A. Pukhov, A. V. Dorofeenko, A. A. Lisyansky, PT-symmetry in optics, Phys.-Uspekhi. 57, (2014) 1063-1082.

[15]. R. El-Ganainy, K. G. Makris, D. N. Christodoulides, Z. H. Musslimani, Theory of coupled optical PT-symmetric structures, Opt. Lett. 32, (2007) 2632-2634.

[16]. A. Guo, G. J. Salamo, D. Duchesne, R. Morandotti, M. Volatier-Ravat, V. Aimez, G. A. Siviloglou, D. N. Christodoulides, Observation of PT-symmetry breaking in complex optical potentials, Phys. Rev. Lett. 103, (2009) 093902.

[17]. C. E. Rüter, K. G. Makris, R. El-Ganainy, D. N. Christodoulides, M. Segev, D. Kip, Observation of parity–time symmetry in optics, Nat. Phys. 6, (2010) 192-195.

[18]. L. Feng, Y. L. Xu, W. S. Fegadolli, M. H. Lu, J. E. Oliveira, V. R. Almeida, Y. F. Chen, A. Scherer, Experimental demonstration of a unidirectional reflectionless parity-time metamaterial at optical frequencies, Nat. Mater. 12, (2013) 108-113.

[19]. Z. J. Wong, Y. L. Xu, J. Kim, K. O'Brien, Y. Wang, L. Feng, X. Zhang, Lasing and anti-lasing in a single cavity, Nat. Photon. 10, (2016) 796-801.

[20]. B. Peng, S. K. Özdemir, F. C. Lei, F. Monifi, M. Gianfreda, G. L. Long, S. H. Fan, F. Nori, C. M. Bender, L. Yang, Parity–time-symmetric whispering-gallery microcavities, Nat. Phys. 10, (2014) 394-398.

[21]. L. Chang, X. S. Jiang, S. Y. Hua, C. Yang, J. M. Wen, L. Jiang, G. Y. Li, G. Z. Wang, M. Xiao, Parity–time symmetry and variable optical isolation in active–passive-coupled microresonators, Nat. Photon. 8, (2014) 524-529.

[22]. J. Zhang, B. Peng, Ş. K. Özdemir, K. Pichler, D. O. Krimer, G. Zhao, F. Nori, Y.-x. Liu, S. Rotter, L. Yang, A phonon laser operating at an exceptional point, Nat. Photon. 12, (2018) 479-484.

[23]. B. Peng, S. K. Ozdemir, M. Liertzer, W. Chen, J. Kramer, H. Yilmaz, J. Wiersig, S. Rotter, L. Yang, Chiral modes and directional lasing at exceptional points, Proc. Natl. Acad. Sci. USA 113, (2016) 6845-6850.

[24]. B. Peng, S. K. Oezdemir, S. Rotter, H. Yilmaz, M. Liertzer, F. Monifi, C. M. Bender, F. Nori, L. Yang, Loss-induced suppression and revival of lasing, Science 346, (2014) 328-332.

[25]. W. Chen, S. Kaya Ozdemir, G. Zhao, J. Wiersig, L. Yang, Exceptional points enhance sensing in an optical microcavity, Nature 548, (2017) 192-196.

[26]. J. Wiersig, Enhancing the Sensitivity of Frequency and Energy Splitting Detection by Using Exceptional Points: Application to Microcavity Sensors for Single-Particle Detection, Phys. Rev. Lett. 112, (2014) 203901.

[27]. J. Wiersig, Structure of whispering-gallery modes in optical microdisks perturbed by nanoparticles, Phys. Rev. A. 84, (2011) 063828.

[28]. J. Wiersig, Sensors operating at exceptional points: General theory, Phys. Rev. A. 93, (2016) 033809.

[29]. J. H. Ren, H. Hodaei, G. Harari, A. U. Hassan, W. Chow, M. Soltani, D. N. Christodoulides, M. Khajavikhan, Ultrasensitive micro-scale parity-time-symmetric ring laser gyroscope, Opt. Lett. 42, (2017) 1556-1559.

[30]. Z. P. Liu, J. Zhang, Ş. K. Özdemir, B. Peng, H. Jing, X. Y. Lü, C. W. Li, L. Yang, F. Nori, Y. X. Liu, Metrology with PT-Symmetric Cavities: Enhanced Sensitivity near the PT-Phase Transition, Phys. Rev. Lett. 117, (2016) 110802.

[31]. W. J. Chen, J. Zhang, B. Peng, S. K. Ozdemir, X. D. Fan, L. Yang, Parity-time-symmetric whispering-gallery mode nanoparticle sensor [Invited], Photonics Res. 6, (2018) A23-A30.

[32]. H. Hodaei, A. U. Hassan, S. Wittek, H. Garcia-Gracia, R. El-Ganainy, D. N. Christodoulides, M. Khajavikhan, Enhanced sensitivity at higher-order exceptional points, Nature 548, (2017) 187-191.

[33]. P. Yeh, M. Hendry, *Optical Waves in Layered Media* (1990), Vol. 43.

[34]. S. Hayashi, H. Kurokawa, H. Oga, Observation of Resonant Photon Tunneling in Photonic Double Barrier Structures, Opt. Rev. 6, (1999) 204-210.

[35]. N. Yamamoto, N. Ohtani, All-Optical Switching and Memorizing Devices Using Resonant Photon Tunneling Effect in Multi-Layered GaAs/AlGaAs Structures, Jpn. J. Appl. Phys. 43, (2005) 1393-1397.

[36]. A. Q. Jian, X. M. Zhang, W. M. Zhu, M. Yu, Optofluidic refractometer using resonant optical tunneling effect, Biomicrofluidics 4, (2010) 043008.

[37]. W. M. Zhu, X. M. Zhang, A. Q. Liu, H. Cai, T. Jonathan, T. Bourouina, A micromachined optical double well for thermo-optic switching via resonant tunneling effect, Appl. Phys. Lett. 92, (2008) 251101.

[38]. A. Q Jian, C. G Wei, L. F Guo, J. Hu, J. Tang, J. Liu, X. M Zhang, S. B Sang, Theoretical Analysis of an Optical Accelerometer Based on Resonant Optical Tunneling Effect, Sensors 17, (2017) 389.

[39]. A. Q. Jian, L. Zou, G. Bai, Q. Q. Duan, Y. X. Zhang, Q. W. Zhang, S. B. Sang, X. M. Zhang, Highly-sensitive cell concentration detection by resonant optical tunneling effect, J. Lightwave Technol. 37, (2019) 2800-2806.

[40]. Y. B. Guo, H. Li, K. Reddy, H. S. Shelar, V. R. Nittoor, X. D. Fan, Optofluidic Fabry–Pérot cavity biosensor with integrated flow-through micro-/nanochannels, Appl. Phys. Lett. 98, (2011) 041104.

[41]. F. Eftekhari, C. Escobedo, J. Ferreira, X. Duan, E. M. Girotto, A. G. Brolo, R. Gordon, D. Sinton, Nanoholes as nanochannels: flow-through plasmonic sensing, Anal. Chem. 81, (2009) 4308-4311.

[42]. X. D. Fan, I. M. White, Optofluidic microsystems for chemical and biological analysis, Nat. Photon. 5,(2011) 591-597.

[43]. A. A. Zyablovsky, A. P. Vinogradov, A. V. Dorofeenko, A. A. Pukhov, A. A. Lisyansky, Causality and phase transitions in PT-symmetric optical systems, Phys. Rev. A 89, (2014) 033808.

[44]. S. Phang, A. Vukovic, S. Creagh, T. Benson, P. Sewell, G. Gradoni, Parity-time symmetric coupled microresonators with a dispersive gain/loss, Opt. Express 23, (2015) 11493-11507.

[45]. H. A. Haus, *Waves and Fields in Optoelectronics* (1984).

[46]. H. Hodaei, M. A. Miri, A. U. Hassan, W. E. Hayenga, M. Heinrich, D. N. Christodoulides, M.Khajavikhan, Parity-time-symmetric coupled microring lasers operating around an exceptional point, Opt. Lett. 40, (2015) 4955-4958.

[47]. A. Mostafazadeh, Spectral singularities of complex scattering potentials and infinite reflection and transmission coefficients at real energies, Phys. Rev. Lett. 102, (2009) 220402.

[48]. H. Hodaei, M. A. Miri, M. Heinrich, D. N. Christodoulides, M. Khajavikhan, Parity-time-symmetric microring lasers, Science 346, (2014) 975-978.

[49]. X. Zhang, Y. Zou, C. An, K. Ying, X. Chen, P. Wang, Sensitive detection of carcinoembryonic antigen in exhaled breath condensate using surface acoustic wave immunosensor, Sens. Actuators B: Chem. 217, (2015) 100-106.

[50]. M. Hasanzadeh, N. Shadjou, Advanced nanomaterials for use in electrochemical and optical immunoassays of carcinoembryonic antigen. A review, Microchim. Acta 184, (2017) 389-414.

[51]. Y. C. Zou, L. Wang, C. Zhao, Y. J. Hu, S. X. Xu, K. J. Ying, P. Wang, C. Chen, CEA, SCC and NSE levels in exhaled breath condensate-possible markers for early detection of lung cancer, J. Breath Res. 7(4), (2013) 047101.

[52]. A. F. Pavlenko, I. V. Chikalovets, A. V. Kurika, V. P. Glasunov, L. V. Mikhalyuk, Y. S. Ovodov, Carcinoembryonic antigen, its spatial structure and localization of antigenic determinants, Tumour Biol. 11(6), (1990) 306-318.

[53]. W. Langbein, No exceptional precision of exceptional-point sensors, Phys. Rev. A. 98, (2018) 023805.

[54]. M. Zhang, W. Sweeney, C. W. Hsu, L. Yang, A. D. Stone, L. Jiang, Quantum Noise Theory of Exceptional Point Amplifying Sensors, arXiv:1805.12001 [quant-ph] (2018).